UNIVERSITI
MALAYSIA
PERLIS

Simulation and Analysis of a Silicon P-I-N Waveguide Based on Electro-Optic Carrier-Depletion Effect

Foo Kui Law*, Mohammad Rakib Uddin and Nur Musyiirah Haji Masri

*Electrical and Electronic Engineering Programme Area, Faculty of Engineering
Universiti Teknologi Brunei, Brunei Darussalam.*

ABSTRACT

This paper provides the analysis of a silicon P-I-N waveguide. The analysis is performed by simulating the said waveguide by applying the electro-optic carrier-depletion effect. Three design parameters have been altered, namely the rib waveguide dimensions, the doping concentration and the electrical contacts distance to the waveguide. The simulation generates the free carrier concentration around a specific region of the waveguide and the waveguide effective index change in response to the voltage applied.

Keywords: PIN Si Waveguide, Electro-Optic, Carrier Depletion.

1. INTRODUCTION

Silicon-based waveguides have been the leading core technology for the development of optical communication and interconnect in photonic integrated circuits. Due to the silicon semiconductor property, it helps to provide us with the cheap and integrable electronic-photonics platform, where portable photonic devices are produced, such as the microring resonators and Mach-Zender modulators.

Recently, a compact waveguide system has been proposed by the usage of silicon nitride (Si_3N_4) and silicon oxynitride (SiON) waveguides [1, 2]. These types of waveguides, however, might not be suitable for electronic-photonic system application since the material absorbs the infrared lights at wavelengths around 1500nm. This absorption can be reduced by exposing the material to high temperature (1,000°C or more), however, this is not compatible with electronic devices due to the high-temperature application.

Based on the research done above, a preferable material used for the construction of waveguide suitable for electronic devices is a silicon-based waveguide. A plasmonic waveguide with metal on top of silicon-on-insulator (SOI) rib waveguide have been demonstrated [3]. Silicon-based slot waveguides have also been realized, with one analyzing the two different slot waveguide configurations [4], another detailing the characterization of high-Q oval resonators based on SOI slot waveguides [5]. Several photonic crystals based on silicon waveguides have been proposed and demonstrated, with one showing a fabrication of an artificial crystal structure containing a full 3D photonic bandgap effect [6], and other showing a slight enhanced optical switch with switching length of 5.2μm [7]. Several all optical high-speed signal switching and processing have also been done using the silicon waveguides for switching mechanisms [8-10].

---

* Corresponding Author: *p20171002@student.utb.edu.bn*

In terms of research applications, most electro-optic devices such as ring modulators and Mach-Zender Interferometers implements the rib-type waveguide with few micrometers in core dimensions, especially those directed logic circuits which use microring resonators [11-13]. Our research analysis on the microring resonator has also incorporated the same type of waveguide [14-18]. This is due to the fact that these types of waveguides are easier to fabricate, and that they are effectively tunable by the application of the electric fields surrounding the waveguides or by thermal effects which affect the waveguide refractive index proportionally.

In this paper, we provide the simulation and analysis of a silicon P-I-N rib-type waveguide which uses free carrier-depletion effect via a change in electrical voltage [19]. The analysis covers the carrier concentration of the rib waveguide when exposed to varying modulation voltage, as well as the resultant waveguide refractive index. The analysis also presents the effect of changing waveguide dimensions, doping concentration as well as the electrical contacts distance (change in an electric field) to the carrier concentration and refractive index of the waveguide. This analysis is essential in a sense that it provides the general idea for the research designers to structural decisions required for their needs in designing effective and reliable photonic devices.

2. WAVEGUIDE STRUCTURE
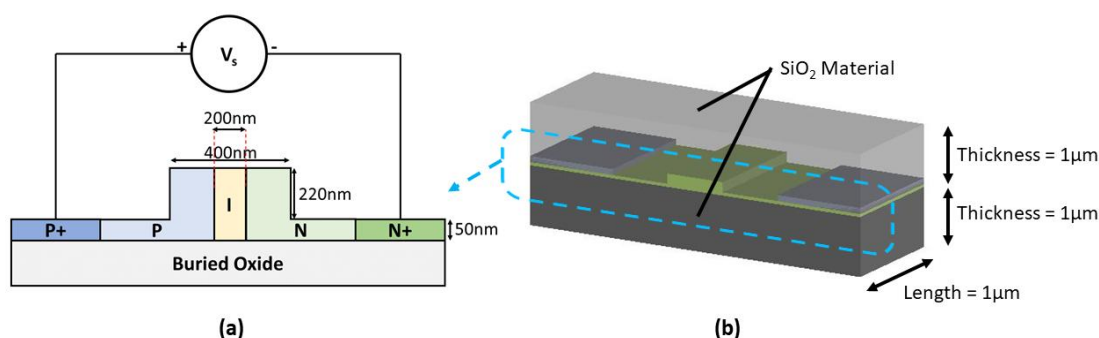
Figure 1. (a) Shows the cross section of the waveguide; (b) Shows the waveguide block structure.

Figure 1(a) shows the cross-section of the ring waveguide while Figure 1(b) shows the block diagram of the waveguide itself of 1µm in length used in the analysis. The rib-type waveguide is deposited on top of the SiO_2 layer of 1µm in thickness as shown in Figure 1(b). The waveguide core dimension is made to be in 400nm width and 220nm in height, with its rib thickness of 50nm. The higher concentration regions of both *p+* and *n+* are doped at 1×10^{18} cm-3 while the lower concentration regions for *p* and *n* are doped at 5×10^{17} cm-3 and 2.5×10^{17} cm-3 respectively. The difference in doping concentration is made so that free carriers from the higher dopant rib waveguide can be injected into the less dopant core waveguide for the apparent change in refractive index at the core waveguide. All of the concentration regions are labeled accordingly in Figure 1, with the intrinsic silicon, is allocated at the center of the waveguide core with 200nm in width. Electrical contacts are placed at the waveguide ribs and are connected to the external electrical source voltage, creating electric fields to engulf the waveguide for electro-optic effects to take place. Another surface oxide SiO_2 is used to place on top of the designed waveguide, resulting the rib waveguide to be encased with SiO_2.

The cross-section rib-type waveguide simulation for this work is done in one of the leading photonics simulation software provided by Lumerical, where the carrier distribution profile generation is done by using the Lumerical DEVICE Solution module and the refractive index

change with respect to the voltage applied profile generation is done in the Lumerical MODE Solution.

3. SIMULATION RESULTS

The simulations for this paper is divided into three parameter changes for the silicon rib-type waveguide, the change in core dimension in terms of its width and height, the dopant concentration of the waveguide and its electrical contacts distance on the rib waveguide. Each simulation will generate its carrier profile generation graphically by Lumerical DEVICE Solution, and its effective index and loss change with voltage by Lumerical MODE Solution.
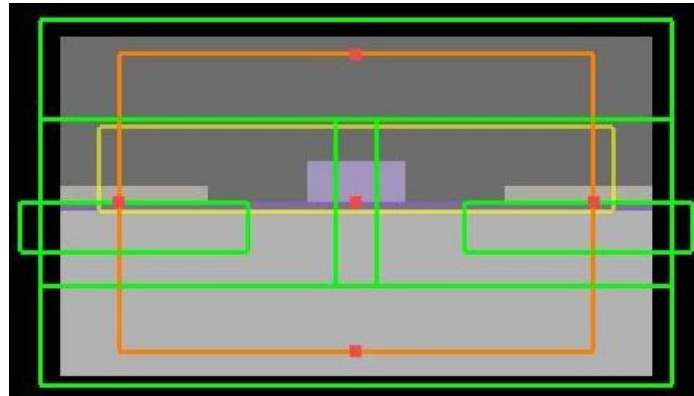

Figure 2. XZ View (cross-section) of the rib-type waveguide in the Lumerical DEVICE simulation environment.

The core waveguide is made of pure silicon as mentioned earlier, where free carriers are doped, and the doping concentration is done in the simulation by using doping region defined in the simulation environment (green boxes in Figure 2). The CHARGE solver region for the software is defined by the orange box and the charge monitor is defined by the yellow box in Figure 2. Once the mesh analysis is done, we observe the charge distribution inside the rib waveguide to be described by Figure 3. Note that this initial simulation is done without any reverse voltage applied to the waveguide ($V_S = 0V$ in Figure 1).
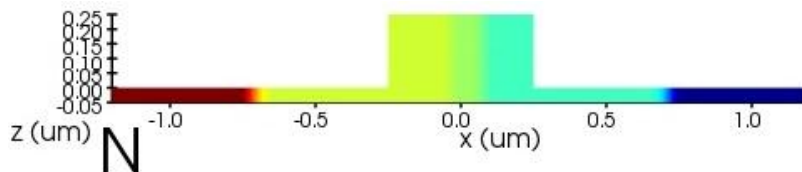
Figure 3. Charge distribution inside the rib-type waveguide at 0V. (red and blue regions are heavily N and P concentrated, while yellow and green regions are lightly N and P concentrated).

Once the charge distribution is obtained, we use Lumerical MODE Solution to generate the waveguide properties in terms of its effective index, waveguide loss, mode of operation, transverse electric polarization for the specific mode (TE polarization) and so on. This information is obtained by using the Eigensolver analysis provided by the software module.
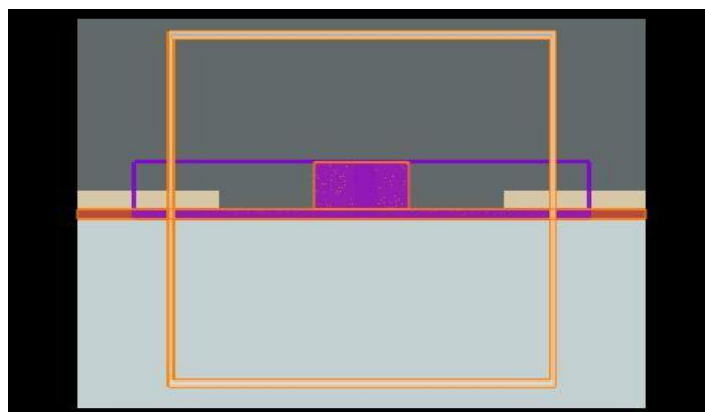
Figure 4. XZ view of the Lumerical MODE simulation environment.

The simulation environment of the rib-type waveguide in MODE solution is as shown in Figure 4, where the Eigenmode solver region is defined by the orange box, and the carrier distribution profile generated from the Lumerical DEVICE earlier is imported to the MODE solution and is represented as the blue region in Figure 4.

We found that the TE polarization fraction operation for the mode 1 at operational wavelength of 1550nm to be 99, suggesting that at mode 1, it is operating at TE transmission. The effective index obtained for the design is 2.77 + j1.71e^{-5} and the waveguide loss for TE mode is 6.01dB/cm. TM mode operation can be obtained at mode 2 with TE polarization fraction of 5 and effective index of 2.44 + j1.61e^{-5}.
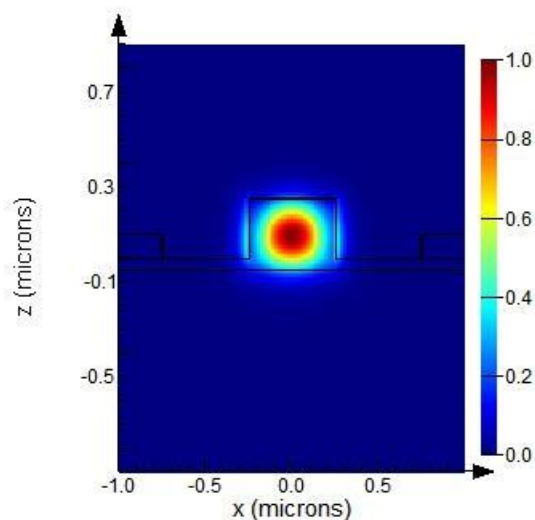
Figure 5. XZ View of the light intensity flowing through the rib-type waveguide.

The next section of this paper sees the various design parameter change of the waveguide core, and the results detailed is the carrier concentration and the effective index change graphs for analysis. The voltage range for the carrier concentration and effective index graph is from 0V to 5V in steps of 0.5V.

3.1 Device Dimension Change

In this section, we analyze the change in carrier concentration at the yellow region in Figure 2 and the refractive index change calculated at the orange region in Figure 4 when we change the

waveguide core's width and height. This will show how the change in waveguide dimensions can affect the carrier distribution and the refractive index of the rib-type waveguide.
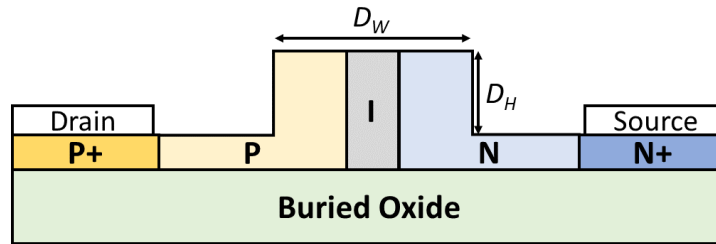

Figure 6. Rib-type waveguide dimension change.

3.1.1. Width Change

In this part of the simulation, we change the width of the waveguide core D_W. The range set for this is from 300nm up to 600nm with steps of 100nm. All other parameters including D_H is kept as detailed by the device structure section of this paper and in Figure 6.
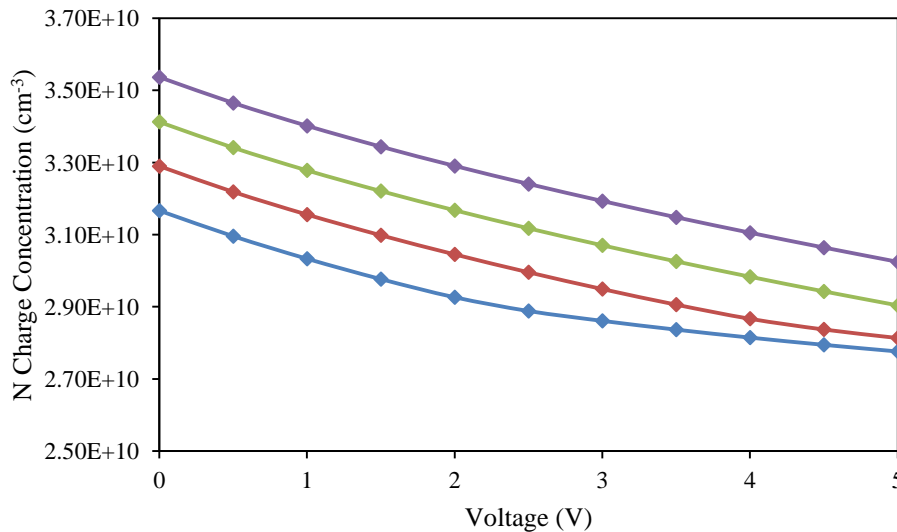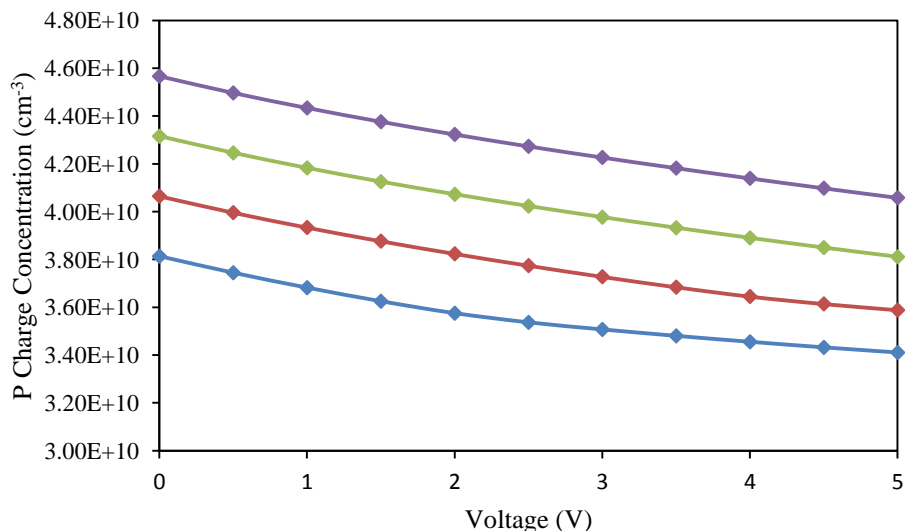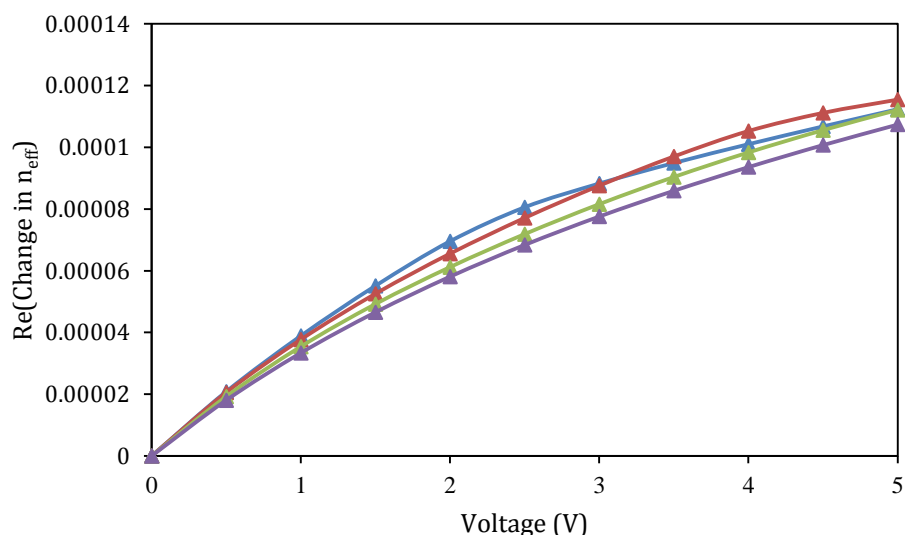

Figure 7. N charge concentration for different core waveguide width. (Blue line: 300nm waveguide width; Orange line: 400nm waveguide width; Grey line: 500nm waveguide width; Yellow line: 600nm waveguide width).

Figure 8. P charge concentration for different core waveguide width. (Blue line: 300nm waveguide width; Orange line: 400nm waveguide width; Grey line: 500nm waveguide width; Yellow line: 600nm waveguide width).

Figure 7 and Figure 8 show the change in charge concentration for different core waveguide width. Blue, orange, grey and yellow color lines represent the concentration change when the core waveguide width is at 300nm, 400nm, 500nm and 600nm respectively. In case of Figure 7, we can see the N charge carrier change inside the core waveguide, while in Figure 8, we can see similar trend in P charge carrier change inside the core waveguide. Based on the result shown, we can conclude that the charge concentration for both N (electrons) and P (holes) charge increases as the core waveguide width increases. It is shown that with bigger width, we can see a little increase in steepness of the graph, suggesting the rate of charge concentration increases with increasing width. This is mainly due to the increasing doping region of the core waveguide at the calculated region in Figure 1.


Figure 9. Change in effective index versus voltage applied. (Blue line: 300nm waveguide width; Orange line: 400nm waveguide width; Grey line: 500nm waveguide width; Yellow line: 600nm waveguide width).

Based on Figure 9, we can see that at 300nm width, there is a higher change in effective index ranging from 0V up to 2.5V, but the rate of change reduced from 2.5V up to 5V, resulting in the change in the effective index by 0.000112296 at 5V. The rate of change in the effective index is at its best when the width is 400nm but reduces when the width is increased more up to 600nm.

3.1.2. Height Change

We vary the height of the waveguide core D_H instead of the width waveguide to observe the effects on the carrier concentration and its effective index. The range set for this is from 200nm up to 300nm with steps of 20nm. As with the previous simulation, all other parameters including D_W is kept as described in the previous section of this paper.
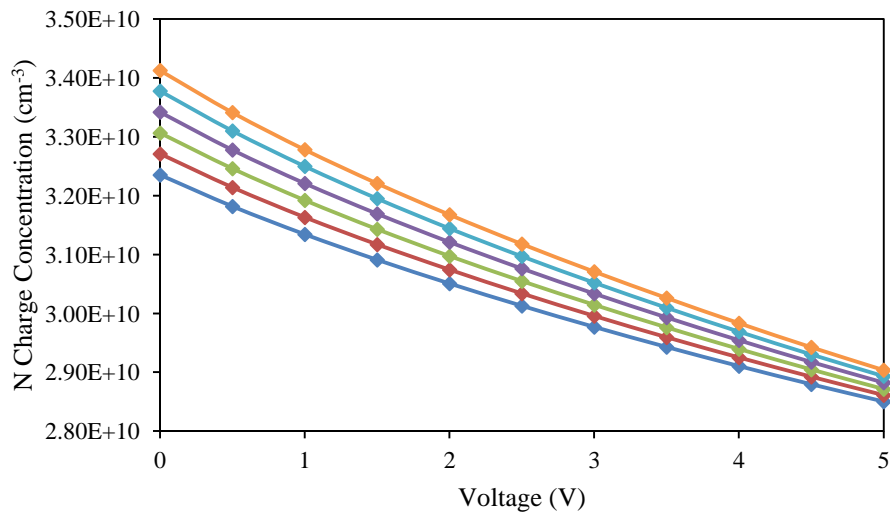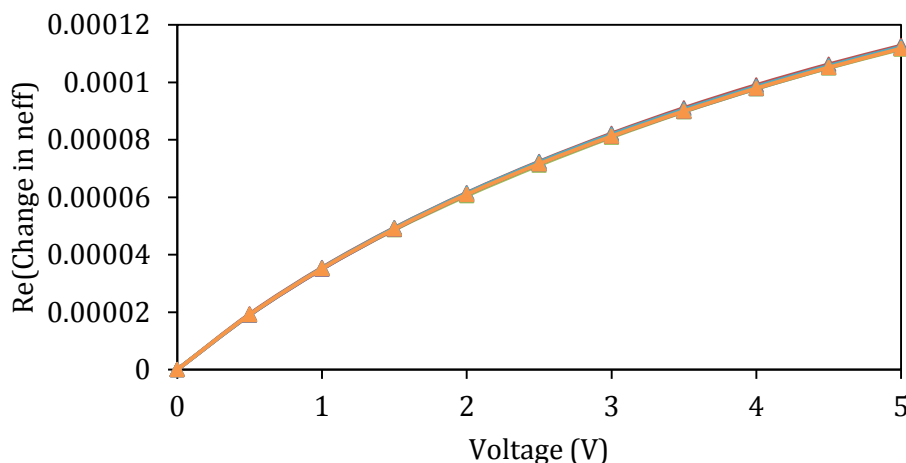

Figure 10. N charge concentration for different core waveguide height. (Dark blue line: 200nm waveguide height; Orange line: 220nm waveguide height; Grey line: 240nm waveguide height; Yellow line: 260nm waveguide height; Light blue line: 280nm waveguide height; Green line: 300nm waveguide height).
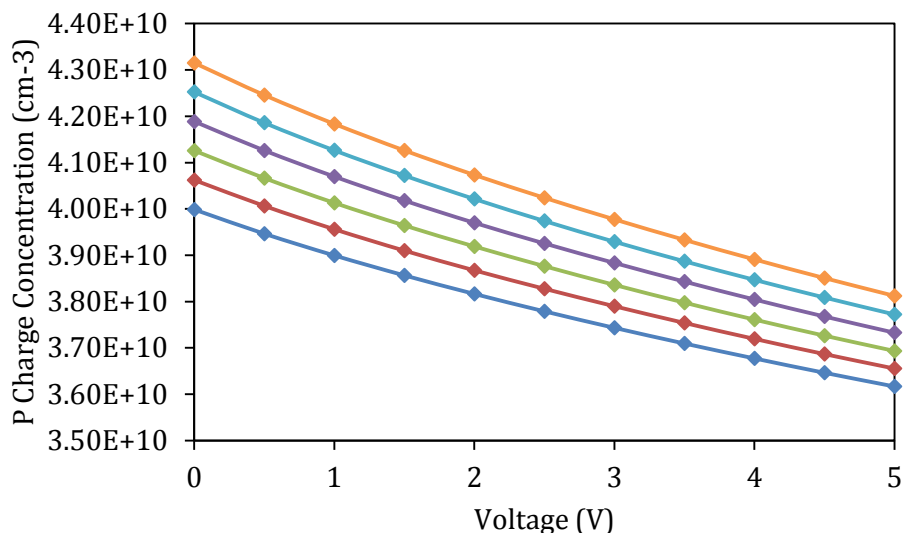
Figure 11. P charge concentration for different core waveguide height. (Dark blue line: 200nm waveguide height; Orange line: 220nm waveguide height; Grey line: 240nm waveguide height; Yellow line: 260nm waveguide height; Light blue line: 280nm waveguide height; Green line: 300nm waveguide height).

Figure 10 as well as Figure 11 show the charge carrier concentration at the core waveguide with the change in core waveguide height. Figure 10 shows the N charge carrier change at the waveguide core while Figure 11 presents the P charge carrier change at the same waveguide core. Six core waveguide height variations are carried out ranging from 200nm up to 300nm in steps of 20nm. The results show that the bigger the height of the core waveguide causes more free carriers to enter the waveguide core as observed in Figure 10 as well as in Figure 11.

Figure 12. Change in effective index versus voltage applied. (Dark blue line: 200nm waveguide height; Orange line: 220nm waveguide height; Grey line: 240nm waveguide height; Yellow line: 260nm waveguide height; Light blue line: 280nm waveguide height; Green line: 300nm waveguide height).

There is no apparent change in the rate of change in the effective index when varying the height of the waveguide core as shown in Figure 12. This is due to the light mode operation is only at TE transmission (horizontal X axis operation).

3.2 Doping Concentration Change

The next part is to change the doping concentration of the waveguide. Both N doping as well as P doping concentration is varied and results in the form of carrier concentration as well as

effective index change is shown. The doping parameters shown in Figure 13 are Do_P and Do_N which corresponds to P and N dopant concentration respectively.
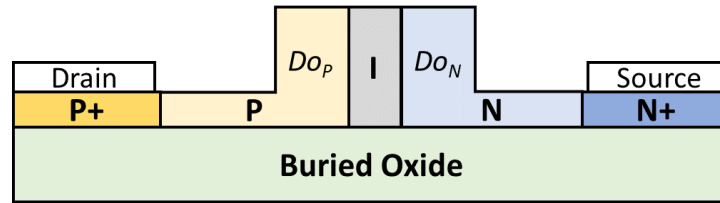

Figure 13. Rib-type waveguide doping concentration change.

3.2.1 N Charge Carrier Change

The range for the change in N charge carrier concentration for the core waveguide Do_N is set from $0.5{\times}10^{17}$ cm-3 up to $2.5{\times}10^{17}$ cm-3 in steps of $0.5{\times}10^{17}$ cm-3. All other parameters are kept as detailed in the device structure section, including the dimensions of the rib waveguide.
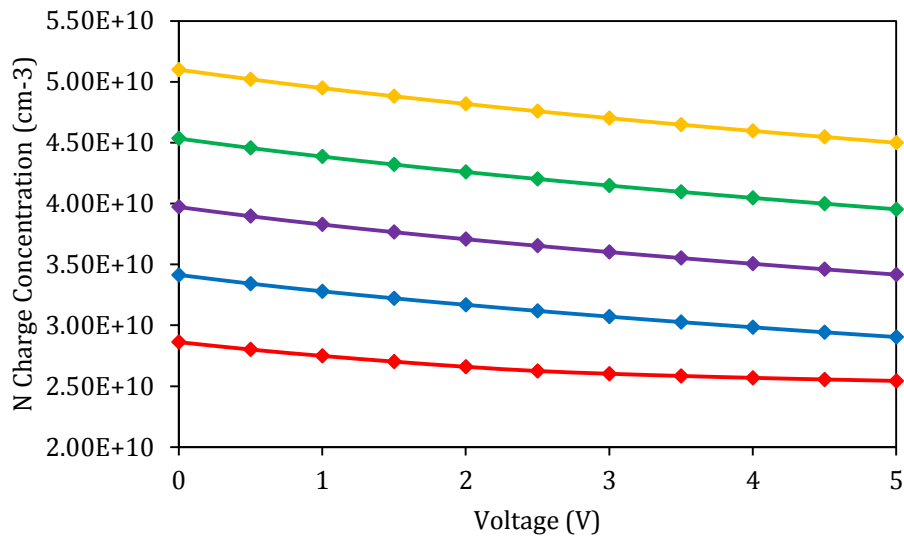
Figure 14. N charge concentration for different N dopant concentration in the waveguide. (Red line: N carrier doped at $0.5{\times}10^{17}$ cm-3; Blue line: N carrier doped at $1.0{\times}10^{17}$ cm-3; Purple line: N carrier doped at $1.5{\times}10^{17}$ cm-3; Green line: N carrier doped at $2.0{\times}10^{17}$ cm-3; Yellow line: N carrier doped at $2.5{\times}10^{17}$ cm-3).
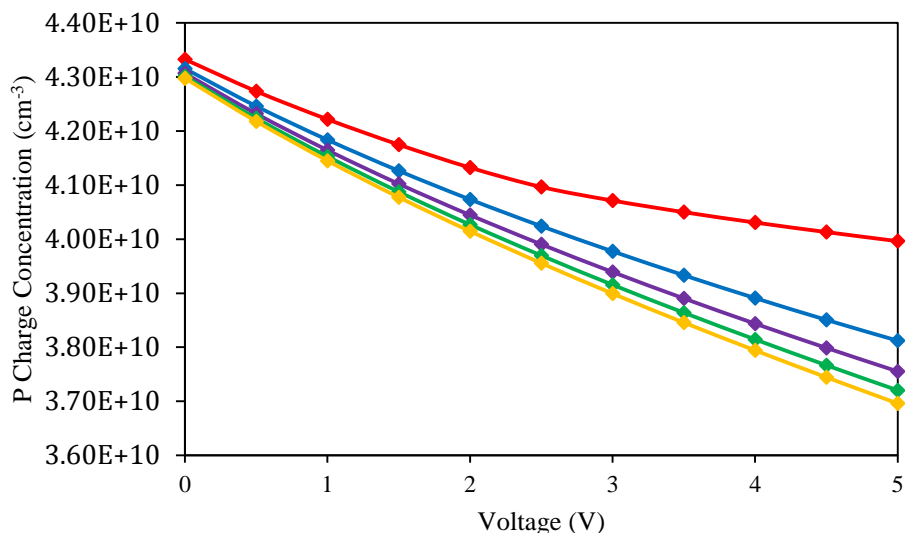
Figure 15. P charge concentration for different N dopant concentration in the waveguide. (Red line: N carrier doped at 0.5×10^{17} cm-3; Blue line: N carrier doped at 1.0×10^{17} cm-3; Purple line: N carrier doped at 1.5×10^{17} cm-3; Green line: N carrier doped at 2.0×10^{17} cm-3; Yellow line: N carrier doped at 2.5×10^{17} cm-3).
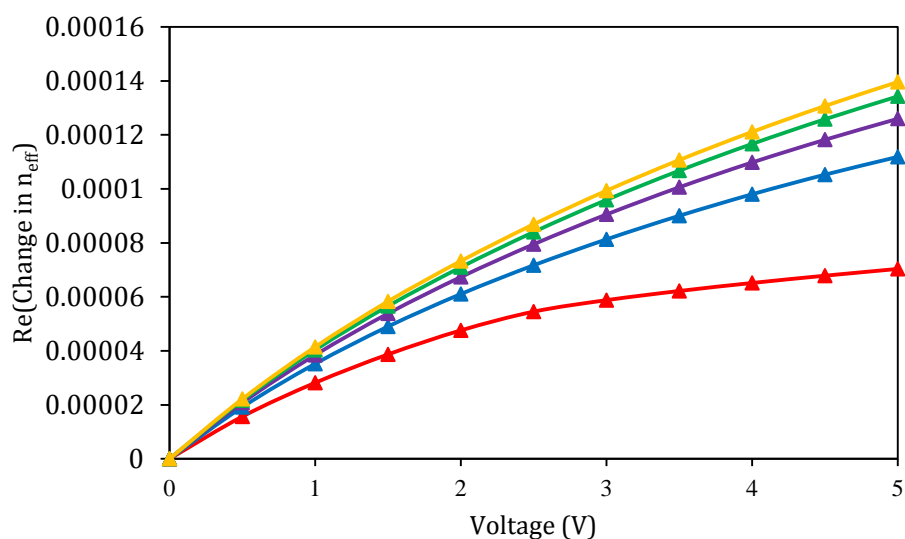

Figure 16. Change in effective index versus voltage applied. (Red line: N carrier doped at 0.5×10^{17} cm-3; Blue line: N carrier doped at 1.0×10^{17} cm-3; Purple line: N carrier doped at 1.5×10^{17} cm-3; Green line: N carrier doped at 2.0×10^{17} cm-3; Yellow line: N carrier doped at 2.5×10^{17} cm-3).

Based on the results shown in Figure 14, as we increase the N dopant concentration, we can observe the linear increase in carrier concentration, and the rate of change in carrier concentration maintains for the most part as demonstrated by the similar gradient shown in Figure 14. This is not the case for the P charge concentration demonstrated in Figure 15 as the change in carrier concentration decreases with the increase of N dopant concentration of the waveguide. The effective index for the core waveguide increases with more N charge doped into it.

3.2.2 P Charge Carrier Change

We now change the P dopant concentration with the range of 1×10^{17} cm-3 up to 5×10^{17} cm-3 in steps of 1×10^{17} cm-3. Similar to all the previous experiments, we set all the other design parameters as in the device structure section.
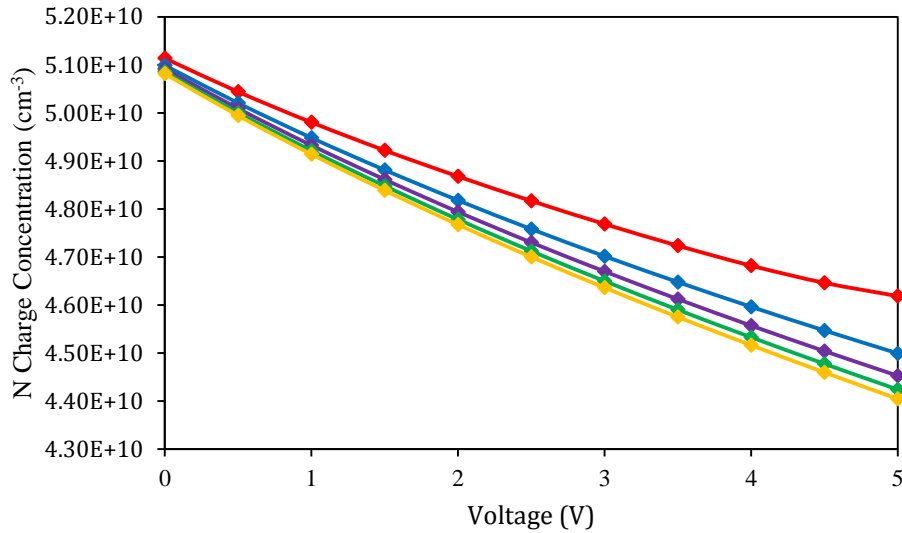
Figure 17. N charge concentration for different P dopant concentration in the waveguide. (Red line: P carrier doped at 1×10^{17} cm-3; Blue line: P carrier doped at 2×10^{17} cm-3; Purple line: P carrier doped at 3×10^{17} cm-3; Green line: P carrier doped at 4×10^{17} cm-3; Yellow line: P carrier doped at 5×10^{17} cm-3).
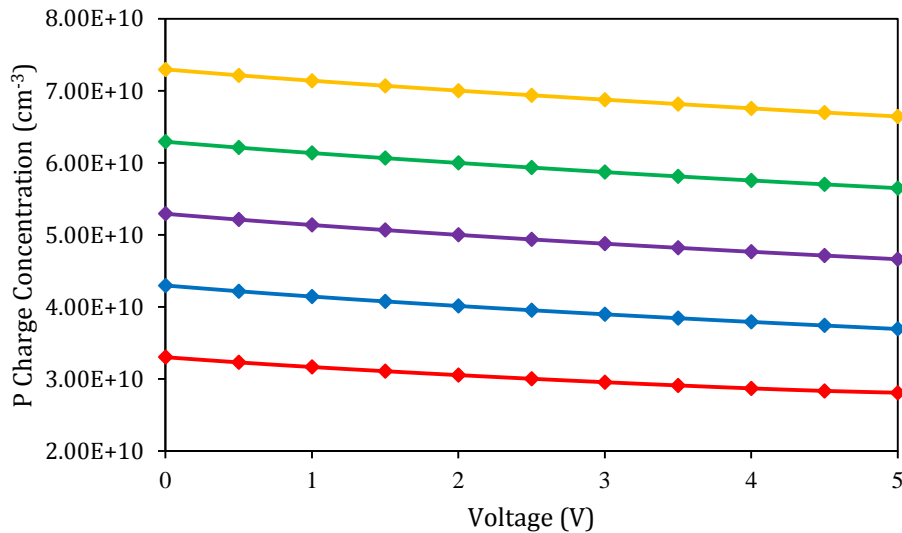
Figure 18. P charge concentration for different P dopant concentration in the waveguide. (Red line: P carrier doped at 1×10^{17} cm-3; Blue line: P carrier doped at 2×10^{17} cm-3; Purple line: P carrier doped at 3×10^{17} cm-3; Green line: P carrier doped at 4×10^{17} cm-3; Yellow line: P carrier doped at 5×10^{17} cm-3).

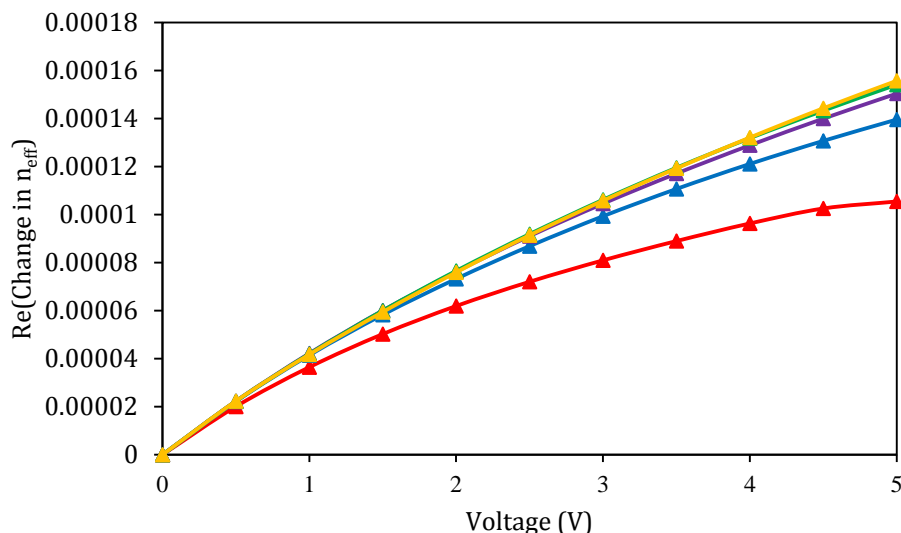**Figure 19.** Change in effective index versus voltage applied. (Red line: P carrier doped at 1×10^{17} cm-3; Blue line: P carrier doped at 2×10^{17} cm-3; Purple line: P carrier doped at 3×10^{17} cm-3; Green line: P carrier doped at 4×10^{17} cm-3; Yellow line: P carrier doped at 5×10^{17} cm-3).

In this section, we can see the opposite of the previous section result in terms of carrier concentration graph. Based on Figure 17, we can see that the N charge carrier concentration decreases as the P doping increases, while the opposite result can be obtained in Figure 18. Figure 19 shows an increased effective index change as the P doping concentration increases.

3.3 Electrical Contacts Distance Change

The final main section in this simulation is the change in electrical contacts distance from the waveguide core, which is labeled as E_D in Figure 20. By changing the electrical contacts distance from the waveguide core, we can vary the electric field intensity exposed to the waveguide, thus effectively change its refractive index.
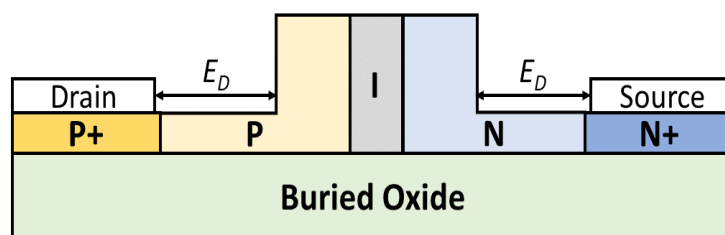
Figure 20. Electrical contacts distance change.

In this part of the simulation, we vary the value of E_D ranging from 100nm up to 500nm in steps of 100nm. All other parameters including waveguide core dimensions as well as the doping concentration are as detailed in the previous section of this paper.
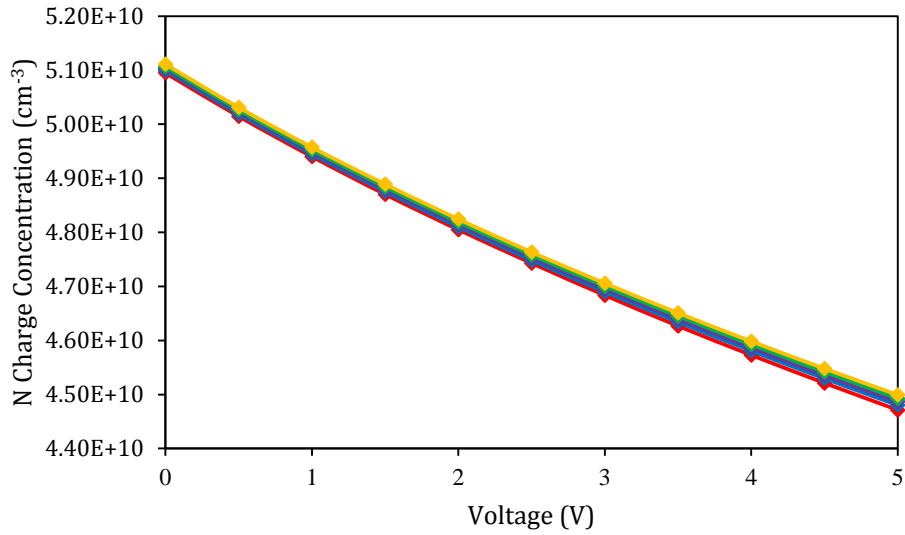
Figure 21. N charge concentration for different electrical contacts distance to the waveguide core. (Red line: $E_D = 500nm$; Blue line: $E_D = 400nm$; Purple line: $E_D = 300nm$; Green line: $E_D = 200nm$; Yellow line: $E_D = 100nm$).
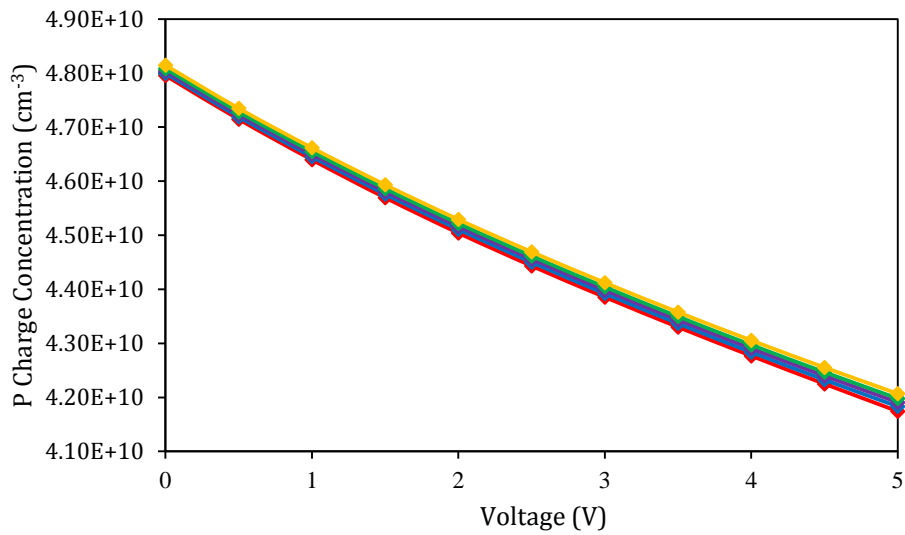
Figure 22. P charge concentration for different electrical contacts distance to the waveguide core. (Red line: $E_D = 500nm$; Blue line: $E_D = 400nm$; Purple line: $E_D = 300nm$; Green line: $E_D = 200nm$; Yellow line: $E_D = 100nm$).
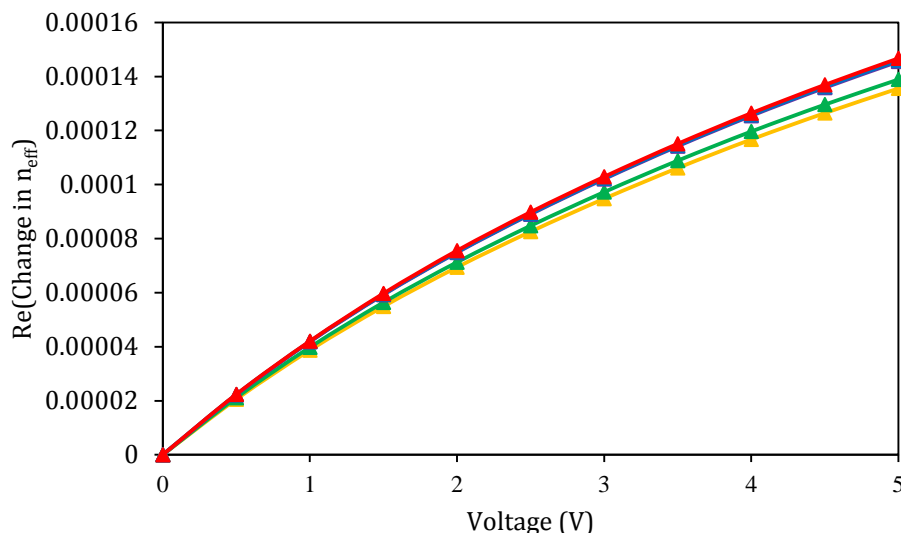
Figure 23. Change in effective index versus voltage applied. (Red line: $E_D = 500nm$; Blue line: $E_D = 400nm$; Purple line: $E_D = 300nm$; Green line: $E_D = 200nm$; Yellow line: $E_D = 100nm$).

Based on the results shown in Figure 21 and Figure 22, there is no apparent change in the graph gradient, thus a constant change in carrier concentration despite the change in electrical contacts distance. The change in effective index shows a slight increase when the contacts are further away from the waveguide core as shown in Figure 23.

4. FUNDAMENTAL THEORY USED IN THE NUMERICAL SIMULATION

The numerical simulation software used for this work utilizes several key equations in order to generate the valid and accurate result for our analysis.

The PIN waveguide carrier concentration is calculated by the Drift-Diffusion equation as presented below [20]:

$$J_n = q\mu_n nE + qD_n \nabla n$$
$$J_p = q\mu_p pE + qD_p \nabla p \tag{1}$$

where $J_{n,p}$ is the net current density (A/cm²), q is the positive electron charge, $\mu_{n,p}$ is the mobility of the free carriers, E is the electric field exposed to the waveguide, $D_{n,p}$ refers to the diffusivity with n and p are the electron and holes densities. These equations represent the summation of carrier drift when electric field is applied and the random thermal diffusion due to the gradient in the density.

The mobility $\mu_{n,p}$ represents the easiness of the free carriers moving inside the waveguide (in this case, the carriers are drifting into the rib waveguide due to attraction to the voltage applied to the rib waveguide). It can be defined together with the diffusivity $D_{n,p}$ through Einstein relation by [21]:

$$D_{n,p} = \mu_{n,p} \frac{k_B T}{q} \tag{2}$$

where k_B is the Boltzmann constant.

The electric field E in Eq. 1 is found by the Poisson's equation [22]:

$$-\nabla.(\varepsilon \nabla V) = q\rho \tag{3}$$

where ε is the dielectric permittivity, V is the electrostatic potential and ρ is the net charge density that can be calculated by:

$$\rho = p - n + C \tag{4}$$

where C is the ionized impurity density in the waveguide.

Drift-Diffusion equations are calculated only on the region where the mesh region is defined in the waveguide (yellow region indicated in Figure 2). These equations generate the carrier concentration profile for both N charge as well as P charge carrier concentration along the yellow region of the waveguide.

The change in effective index with respect to the voltage applied is done by converting the obtained charge carrier concentration profile generated earlier to the change in refractive index. This is done by utilizing the silicon model demonstrated by the experiments carried out by Soref *et al.* [23]:

$$\Delta n = (dn\_Ap)(\Delta P)^{dn\_Ep} + (dn\_An)(\Delta N)^{dn\_En}$$
$$\Delta \alpha = (d\alpha\_Ap)(\Delta P)^{d\alpha\_Ep} + (d\alpha\_An)(\Delta N)^{d\alpha\_En} \tag{5}$$

where Δn is the change in refractive index, $\Delta \alpha$ is the variation in absorption coefficient in cm^{-1}, ΔP and ΔN is the change in hole and electron concentration respectively in cm^{-3}.

Based on the experiments carried out by Soref *et al.*, at 1550nm operating wavelength, the silicon model equations include the coefficients as follow:

$$\Delta n = (-8.5 \times 10^{-18})(\Delta P)^{dn\_Ep} + (-8.8 \times 10^{-22})(\Delta N)^{dn\_En}$$
$$\Delta \alpha = (6 \times 10^{-18})(\Delta P)^{d\alpha\_Ep} + (8.5 \times 10^{-18})(\Delta N)^{d\alpha\_En} \tag{6}$$

5. CONCLUSION

This paper has presented the simulation and analysis of a silicon P-I-N rib-type waveguide. Simulations of the said waveguide with the varying voltage applied to the waveguide electrical contacts have been performed, and graphs have been plotted to present the results. Three design parameters have been simulated to determine its effect on the waveguide carrier concentration and its effective index change. The simulations have presented interesting results in a sense that we can directly see the impact of each of the design parameters into the result and efficiency of the P-I-N waveguide. Several key points can be derived from the simulation

results which can be proved to be useful. One of such key points is that the width of the waveguide affects the effective index where a 400nm proves to generate the highest rate of change in the effective index at the range of 0V to 5V. While the change in effective index at the waveguide core's width of 300nm has the highest change in effective index up to 2.5V, the trend did not reach during the voltage range of 2.5V up to 5V, thus as an overall result, 400nm width has the highest rate of change ranging from 0V up to 5V. We can also confirm that increasing the dopant concentration can improve the effective index change of the waveguide. Electrical contacts have been shown to contribute a small effect in increasing the waveguide rate of change in the effective index.

REFERENCES

[1]   G.-L. Bona, R. Germann & B. J. Offrein, SiON high-refractive-index waveguide and planar lightwave circuits, IBM Journal of Research and Development **47** (2003) 239-249.

[2]   M. J. Kobrinsky, B. A. Block, J.-F. Zheng, B. C. Barnett, E. Mohammed, M. Reshotko, *et al.* On-Chip Optical Interconnects, Intel Technology Journal **8** (2004).

[3]   D. Dai & S. He, A silicon-based hybrid plasmonic waveguide with a metal cap for a nano-scale light confinement, Optics express **17**(2009) 16646-16653.

[4]   P. Sanchis, J. Blasco, A. Martínez & J. Martí, Design of silicon-based slot waveguide configurations for optimum nonlinear performance, Journal of Lightwave Technology **25** (2007) 1298-1305.

[5]   T. Baehr-Jones, M. Hochberg, C. Walker & A. Scherer, High-Q optical resonators in silicon-on-insulator-based slot waveguides, Applied Physics Letters **86** (2005) 081101.

[6]   S. Noda, K. Tomoda, N. Yamamoto & A. Chutinan, Full three-dimensional photonic bandgap crystals at near-infrared wavelengths, Science **289** (2000) 604-606.

[7]   D. M. Beggs, T. P. White, L. O'Faolain & T. F. Krauss, Ultracompact and low-power optical switch based on silicon photonic crystals, Optics letters **33** (2008) 147-149.

[8]   Ö. Boyraz, P. Koonath, V. Raghunathan & B. Jalali, All optical switching and continuum generation in silicon waveguides, Optics Express **12** (2004) 4094-4102.

[9]   K. Yamada, H. Fukuda, T. Tsuchizawa, T. Watanabe, T. Shoji & S. Itabashi, All-optical efficient wavelength conversion using silicon photonic wire waveguide, IEEE Photonics Technology Letters **18** (2006) 1046-1048.

[10]   A. Martínez, J. Blasco, P. Sanchis, J. V. Galán, J. García-Rupérez, E. Jordana, *et al.*, Ultrafast all-optical switching in a silicon-nanocrystal-based silicon slot waveguide at telecom wavelengths, Nano letters, **10** (2010) 1506-1511.

[11]   C. Qiu, W. Gao, R. Soref, J. T. Robinson & Q. Xu, Reconfigurable electro-optical directed-logic circuit using carrier-depletion micro-ring resonators, Optics letters **39** (2014) 6767-6770.

[12]   L. Zhang, R. Ji, L. Jia, L. Yang, P. Zhou, Y. Tian, *et al.*, Demonstration of directed XOR/XNOR logic gates using two cascaded microring resonators, Optics letters **35** (2010) 1620-1622.

[13]   Y. Tian, L. Zhang, R. Ji, L. Yang, P. Zhou, H. Chen, *et al.*, Proof of concept of directed OR/NOR and AND/NAND logic circuit consisting of two parallel microring resonators, Optics letters **36** (2011) 1650-1652.

[14]   L. F. Kui & M. R. Uddin, Photonic microring resonator modulated resonance response analysis, Optical and Quantum Electronics **49** (2017) 275.

[15]   F. Law, M. R. Uddin, H. Hashim & Z. Hamid, Simulation and demonstration of electro-optic digital logic gates based on a single microring resonator, Optical and Quantum Electronics **49** (2017) 413 2017.

[16]   M. R. Uddin, T. K. Siang, N. Munarah, M. Norfauzi, N. Ahmed & M. Salam, Quality Analysis of a Photonic Micro-ring Resonator, in Computer and Communication Engineering (ICCCE), International Conference on, **2016** (2016) 382-385.

[17] M. R. Uddin, S. Newaz, A. Hamid, Z. Haji & Y. H. Won, Temperature Characteristics of Silicon-Polymer Hybrid Material Photonic Resonator, in Key Engineering Materials (2017) 143-147.

[18] M. R. Uddin, B. Nakarmi & Y. H. Won, Waveguide side-wall angle dependant resonance of a Si micro ring-resonator, in Lasers and Electro-Optics Pacific Rim (CLEO-PR), 2015 11th Conference on (2015) 1-2.

[19] B. Li, G. Li, E. Liu, Z. Jiang, C. Pei & X. Wang, 1.55 µm reflection-type optical waveguide switch based on SiGe/Si plasma dispersion effect, Applied physics letters, **75** (1999) 1-3.

[20] X. Prieto-Blanco, Electro-diffusion equations of monovalent cations in glass under charge neutrality approximation for optical waveguide fabrication, Optical Materials **31** (2008) 418-428.

[21] B. Van Zeghbroeck, Principles of semiconductor devices, Colarado University (2004).

[22] M. V. Fischetti & W. G. Vandenberghe, Scattering with ionized impurities, in Advanced Physics of Electron Transport in Semiconductors and Nanostructures ed: Springer (2016) 315-325.

[23] R. Soref & B. Bennett, Electrooptical effects in silicon,) IEEE journal of quantum electronics **23** (1987) 123-129.